



# Electric explosion of amorphous iron alloy ribbons in water and in ethylene glycol

K. Lázár<sup>1,a)</sup>, L. K. Varga<sup>2</sup>, V. Kovács-Kis<sup>3</sup>, S. Stichleutner<sup>1</sup>, A. Tegze<sup>1</sup>, Z. Klencsár<sup>1</sup>

<sup>1</sup>EKBI, Centre for Energy Research, ELKH, Budapest, Konkoly Thege Miklós út, 29-33, Budapest 1121, Hungary

<sup>2</sup>Wigner Research Centre, ELKH, Budapest, Konkoly Thege Miklós út, 29-33, Budapest 1121, Hungary

<sup>3</sup>MFA, Centre for Energy Research, ELKH, Budapest, Konkoly Thege Miklós út, 29-33, Budapest 1121, Hungary

<sup>a)</sup>Address all correspondence to this author. e-mail: lazar.karoly@ek-cer.hu

Received: 24 July 2022; accepted: 29 September 2022

Electric explosions of amorphous ribbons ( $\text{Fe}_{45}\text{Co}_{45}\text{Zr}_7\text{B}_3$  HITPERM,  $\text{Fe}_{73.5}\text{Si}_{15.5}\text{B}_7\text{Nb}_3\text{Cu}_1$  FINEMET, and bulk amorphous  $\text{Fe}_{71.6}\text{Mn}_{0.6}\text{Si}_{3.4}\text{C}_{12.3}\text{B}_{12.2}$ ) were studied in water and for the bulk amorphous alloy in ethylene glycol, in order to study whether the amorphous state can be preserved in the process. Formed products were collected and analyzed by Scanning Electron Microscopy, X-ray diffraction, Mössbauer spectroscopy, and High-Resolution Transmission Electron Microscopy. Chemical reactions have taken place in large extent between melted and evaporated components of ribbons and the decomposed cooling media. The oxidation reactions removed quickly the glass-forming elements (Zr, B, Si) from the metallic particles. Oxides were formed both on surface of globules and in separate phases from evaporated components. The amorphous state was partly retained in FINEMET, and to a greater extent in bulk amorphous alloy. Chemical interactions were more limited in ethylene glycol and carbon atoms formed from the decomposed coolant contributed to stabilization of amorphous phase.

## Introduction

The process of the electric explosion of wires (EEW) has attracted attention since the middle of the last century as, e.g., organization of series of conferences related to various aspects of the phenomenon attests from the early times [1]. Other terms, like wire explosion process, WEP, or pulsed wire discharge, PWD, are also used alternatively. The interest has been renewed in connection with preparation of nanoparticles [2]. Further details of the processes are also studied in detail recently (e.g., the physical background and various regimes of the process [3], electric circuit analysis [4]).

In a brief approach, exposure of a thin metallic wire to a strong current pulse results in melting, formation of small droplets, and evaporation of the metal afterwards. In case of using a sufficiently strong energy pulse, the current flow can be sustained via the neighboring plasma after having the conduction of current ceased through the molten metal. Depending on the surrounding media (vacuum, gaseous, or liquid) additional chemical reactions may take place in the exploding neighboring gaseous media which collapse quickly. All the processes are completed within a few nanoseconds. Further details

are also reported recently (e.g., description of early stages with emergence of different shock waves [5], the various discharge channels [6], or comparison of EEW of a Cu wire in air, in water, and in half-air & half-water combination [7]).

There is a wide room for chemical interactions with the surrounding media. For instance, various carbides or nitrides can be prepared in carbon or nitrogen-rich ambient media (e.g., [8], tungsten carbide [9], aluminum nitride [10]). The formed particles can be stabilized by surfactants [11], or alloys can be prepared with exploding twisted metal wires [12]. The emphasis can be put to preparation of side products as well, e.g., fabrication of fullerenes, carbon nanotubes, and nanodiamonds can be achieved in carbon-rich media [13].

It should be mentioned that preparation of nanoparticles with fast cooling of evaporated and molten metal droplets can also be performed via related methods, namely with spark erosion [14], or with pulsed laser ablation [15].

In our related previous communication, EEW of iron and alloy wires was studied in various media (water, paraffin oil, ethylene glycol, siloxane) with particular attention to reactions with the ambient media. The products were separated into coarse

and fine fractions (in ca. 95% vs. 5% mass distribution). Reactions of primary components of wires with the ambient liquids were deduced from composition changes found in comparison of the primary wire and solidified molten droplets (the main component of coarse fraction) and were also proven directly by analyzing the primary reaction products present in the fine fraction [16].

Preparation of amorphous metallic nanoparticles can also be attempted by starting directly from amorphous metallic wires exposing them to EEW. The process can be distinctly different since the specific conductivity in amorphous metals is 2–3 order of magnitude less than in crystalline wires [17]. The success of preservation of the amorphous state is strongly connected to the extent of maintaining the composition and the high cooling rate. Synthesis of magnetic nanoparticles was performed with EEW of  $(\text{Co(Fe)})_{72.5}\text{Si}_{12.5}\text{B}_{15}$  and  $\text{Fe}_{78}\text{Si}_9\text{B}_{13}$  amorphous wires in argon. The starting wires (with 0.22–0.14 mm diameters) were prepared by the so-called in-water-rotating-spinning method [18]. After the EEW process, ca. 20% of the product was retrieved in amorphous phase, with certain increase of the Si and B contents compared to the starting composition [19]. Higher amorphous content can be achieved with laser ablation of bulky amorphous ingots. A few nanometer size particles are formed with short (picosecond) laser pulses applied to  $\text{Fe}_{78}\text{Si}_9\text{B}_{13}$  metallic glass target in appropriate, carbon-containing liquid media from which carbon may be dissolved into the metallic phase [20, 21]. Considerably larger, a few micrometer size particles can be prepared from various metallic glass ingots with spark erosion (localized pulsed electrical discharge) [14].

Similarly to wires, ribbons can also be exposed to EEW, since the cross sections of melt-spun ribbons are in the same range than those of thin wires. Thus, in the present report, we give an account on characterization of products formed from crystalline and amorphous ribbons in the process of EEW. In particular, melt-spun crystalline  $\text{Fe}_{50}\text{Co}_{50}$ , and amorphous  $\text{Fe}_{45}\text{Co}_{45}\text{Zr}_7\text{B}_3$  (HITPERM, Fe:Co with 1:1 atomic ratio with addition of glass-forming zircon and boron),  $\text{Fe}_{73.5}\text{Si}_{15.5}\text{B}_7\text{Nb}_3\text{Cu}_1$  (FINEMET) were exploded in water and bulk amorphous  $\text{Fe}_{71.6}\text{Mn}_{0.6}\text{Si}_{3.4}\text{C}_{12.3}\text{B}_{12.2}$  ribbons (prepared by adding boron to cast iron) were vaporized both in water and in ethylene glycol. Products were collected in two fractions. The coarse fraction was precipitated within one day, whereas the fine fraction was primarily composed from the suspended products floating in the cooling media for several days. The coarse fraction was mostly composed from instantly frozen melted larger and smaller globules, whereas the fine fraction consists dominantly from products of reactions of evaporated metals with the quenching liquids. The estimation of the extent of the conservation of the amorphous state of the original ribbons was in focus. Furthermore, attention was also paid to tracking the changes of compositions both in the larger globules, and in the newly formed

nanosized components. The morphology of products was characterized by Scanning Electron Microscopy (SEM), and phases were analyzed by X-ray diffraction (XRD) and  $^{57}\text{Fe}$  Mössbauer spectroscopy. The structure and composition of products in the nanometer size range were revealed from High-Resolution Transmission Electron Microscopy (HRTEM) observations.

## Results and discussion

### $\text{Fe}_{50}\text{Co}_{50}$ in water

The primary reason to perform EEW on crystalline  $\text{Fe}_{50}\text{Co}_{50}$  ribbon was to check whether nanocrystalline structure can be formed during quick quenching from the crystalline metallic ribbon without containing any glass-forming element.

*Morphology* of products was revealed from SEM studies. Both spherical and cornered particles were found in the images. The elemental analysis reveals the presence of 25–45 wt % oxygen on their surfaces. The starting Fe to Co 1:1 atomic ratio is approximately retained in the products. The corresponding images are presented in Fig. SSEM1 (Supplementary Information, SI).

*XRD diffractograms* demonstrate the dominant presence of crystalline phases both before and after EEW. Completion of EEW process is manifested in the appearance of the oxide phase with reflections of wüstite structure, displaying smaller nanosized domains with coherent scattering (see the corresponding diffractograms in Fig. SXRD1 (SI)).

*The Mössbauer spectrum* of the starting  $\text{Fe}_{50}\text{Co}_{50}$  ribbon displays sharp peaks of a magnetically ordered sextet confirming the crystalline state on 91% spectra area with additional 9% wüstite contribution (Fig. 1 top). The dominant sextet can adequately be described with random distribution of Co and Fe atoms in bcc structure where the magnitude of inner local magnetic fields ( $B_{\text{hf}}$ ) depends on the number of nearest neighbors ( $N_{\text{nn}}$  [22, 23])

$$(B_{\text{hf}}(N_{\text{nn}})) = B_{\text{hf},0} + N_{\text{nn}} \times \Delta B_{\text{hf},\text{nn}} \quad (1)$$

(further details of decomposition can be found in the supporting information—SMB Table 1).

The EEW process results in oxidation of iron and cobalt in significant extents (c.a. 50% as for Fe). The non-oxidized part exhibits similar distribution of magnetic fields as the original ribbon (Fig. 1 bottom). Certain depletion of iron can be observed in the metallic part (in the contribution of sextet), compared to the starting Fe to Co 1:1 ratio, since the extent of formation enthalpy of iron oxides exceeds those of cobalt oxides (for FeO 272 kJ/mol, for CoO 238 kJ/mol, and further on, more stable  $\text{Fe}_3\text{O}_4$  (1121 kJ/mol) may also form [24]). In correspondence, signals of FeO doublets and additional  $\text{Fe}^{3+}$  component can be included to cover the center of this

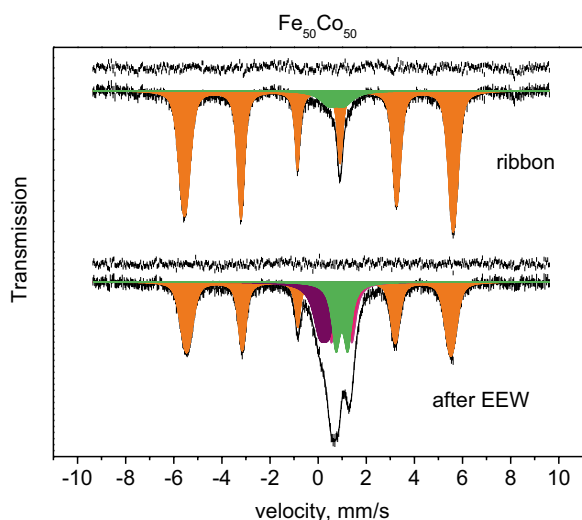


**Figure 1:** Mössbauer spectrum of the starting  $\text{Fe}_{50}\text{Co}_{50}$  ribbon (top) and the spectrum obtained on products after EEW (bottom, sextet of FeCo alloy in orange,  $\text{Fe}^{2+}$  doublets of wüstite in green and pink,  $\text{Fe}^{3+}$  in purple).

spectrum for the remaining ~ 50% of the spectral area (tabulated data of decomposition are compiled in SMb Tables 1 and 2, SI).

### HRTEM observations

The progress of oxidation processes is also obvious from the analysis of HRTEM images. The presence of two structures, octahedral cubic ( $\text{FeO}$ , wüstite) and spinel ( $\text{Fe}_3\text{O}_4$ , magnetite), is revealed [Fig. 2(a, b, c)]. The oxides are mixed Fe,Co oxides as the elemental maps are shown (Fig. 2, bottom part). It is worth to mention that complete oxidation of small particles may take place with preserving the spherical shape. In short, two main observations can be noticed at the first glance for the EEW of crystalline  $\text{Fe}_{50}\text{Co}_{50}$  ribbons. First, oxidation proceeds in part due to interaction with water for both cobalt and iron constituents, and second, the crystalline structure is preserved both for the original metallic cores in the globules and for the formed oxidic products.

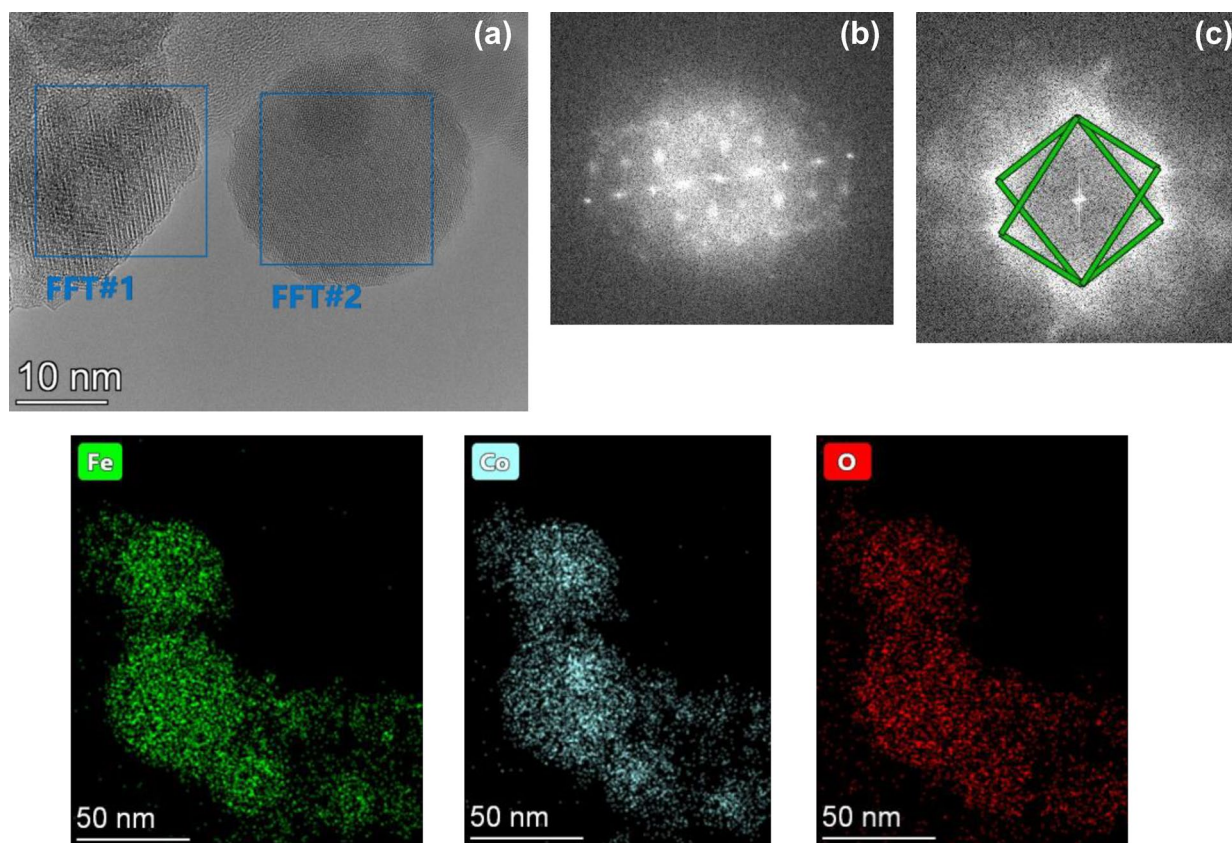


**Figure 2:** HRTEM image on particles of products of EEW with  $\text{Fe}_{50}\text{Co}_{50}$ , a), top left; fast Fourier transforms of region #1 with characteristic reflections of magnetite [110] at 4.8 Å, b); and on region #2 characterizing wüstite structure, with [110] reflections at 2.5 Å, c). Respective elemental distributions of Fe, Co, and O are displayed in the bottom part.

### Amorphous $\text{Fe}_{45}\text{Co}_{45}\text{Zr}_7\text{B}_3$ (HITPERM) in water

In the composition of the starting amorphous ribbon, the atomic Fe:Co = 1 ratio is maintained for comparison to the previous  $\text{Fe}_{50}\text{Co}_{50}$ , with addition of glass-forming Zr and B in sufficient extents.

*Morphology and surface compositions* were derived from SEM analysis. The product of EEW process is composed from both angular and spherical particles. The oxidation is also expressed, in particular for zirconium (see supporting information Fig. SSEM2).

XRD diffractometry reveals that the EEW process results in crystallization. The composition change may also significantly promote the crystallization by removing the glass-forming zirconium from the metallic phase with oxidation (formation enthalpy of ZrO is large, 1097 J/mol [24]). See the corresponding XRD spectra in the supporting information in Fig. SXRD2.

#### Mössbauer spectroscopy

The spectra of the starting ribbon and that of the products collected after EEW are shown in Fig. 3. Their interpretation is in full correspondence with results of XRD analysis. As for the first, starting amorphous state, the spectrum of the as-cast ribbon can be described with a distribution of hyperfine magnetic fields centered at ~30.0 T (HITPERM alloys with similar composition exhibit similar distribution (e.g., [25]).

The EEW process results significant changes in the shape of spectrum. A simple visual comparison of the spectra of the starting amorphous ribbon (Fig. 3 left, top) and the products after the EEW (Fig. 3 left, bottom) indicates that crystallization

has taken place in the metallic phase, the sextet lines are sharp in the spectrum of products. More detailed decomposition of this spectrum attests that 74% of spectral area can be described with a random binomial distribution of Fe and Co in the bcc alloy with Eq. 1, similarly to the spectra of the previous case, to the  $\text{Fe}_{50}\text{Co}_{50}$  ribbon. The corresponding  $\langle B_{\text{hf}} \rangle$ ,  $B_{\text{hf},0}$ , and  $\Delta B_{\text{hf},\text{nn}}$  parameters of Eq. 1 are 34.6, 29.4, and 0.62 Tesla, respectively. The remaining 26% spectral contribution can be attributed to  $\text{Fe}^{2+}$  and  $\text{Fe}^{3+}$  doublets originated from various oxides with isomer shift and quadrupole splitting pairs, of 0.95, 1.01, and 0.32, 0.69 mm/s values, respectively.

HRTEM study was performed on the fine fraction of products of EEW of the HITPERM ribbon. The presence of oxides in significant extents was observed both with electron diffraction and elemental analysis. Enrichment of iron oxides on the surface layers can be observed, whereas the distribution of cobalt remains more homogeneous (Fig. 4).

Short summary for HITPERM—results obtained with various methods are in good correspondence: complete loss of the starting amorphous structure and oxidation of components in significant extents are observed.

### $\text{Fe}_{73.5}\text{Si}_{15.5}\text{B}_7\text{Nb}_3\text{Cu}_1$ (FINEMET in water)

The next amorphous ribbon exposed to EEW was FINEMET. In this alloy, the glass-forming components are silicon and boron. The enthalpy for oxide formation of silicon is high (for  $\text{SiO}_2$  910 kJ/mole [24]). A plain experimental observation is in correspondence with strong oxidation since the EEW process is rather vivid in water.

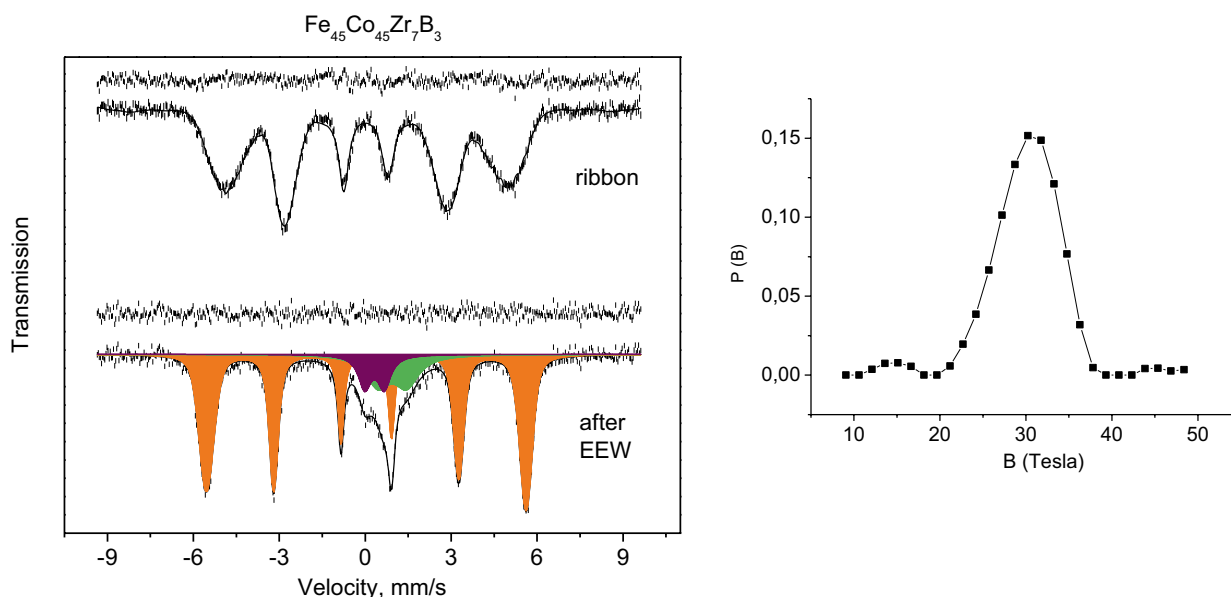


**Figure 3:** Mössbauer spectrum of the starting  $\text{Fe}_{45}\text{Co}_{45}\text{Zr}_7\text{B}_3$  amorphous ribbon (left, top), and the corresponding distribution of hyperfine magnetic fields (right side). The spectrum of the products after EEW is shown in the left bottom part (FeCo alloy in orange, oxides of iron in green and purple).



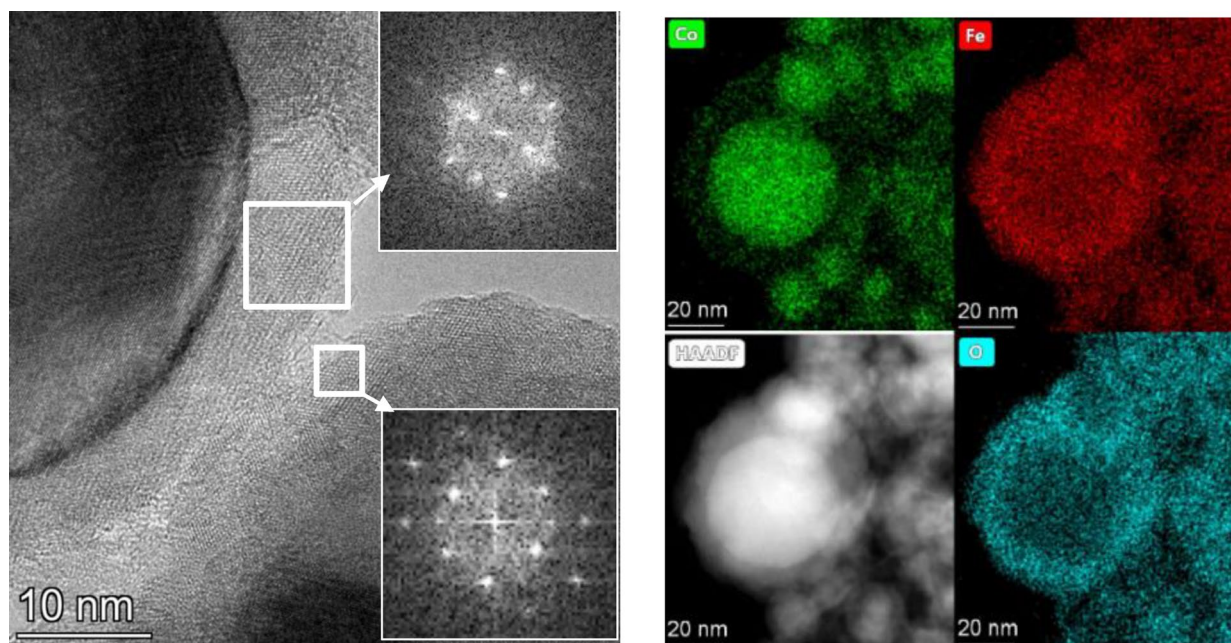


**Figure 4:** HRTEM image obtained on products of EEW of HITPERM alloy. Parts of spherical particles (left), according to the FFTs on the areas indicated by white squares, have magnetite structure: upper and lower FFTs are  $[-112]$  and  $[1-14]$  zone axis magnetite, respectively. Elemental distributions of Co, Fe, and oxygen are displayed on the right (HAADF: High-Angle Annular Dark field).

*Morphology and surface analysis by SEM* reveals the presence of products with various extents of oxidation. Both spherical and cornered particles are present (see the images and the corresponding analyses in Fig. SSEM 3, SI).

*Structure and elemental distribution* in nanoparticles was studied with *HRTEM*. Large melted and solidified globules immersed to oxides formed mostly from vaporized Si and boron are present (Fig. SHRTEM 1, SI). The elemental distribution is in accordance, and the presence of oxygen and silicon is homogeneous in the first approach, (Fig SHRTEM 1, center, SI) whereas iron and copper agglomerate to islands (Fig. SHRTEM 1, right, SI).

### Mössbauer spectroscopy

The spectrum of the starting amorphous FINEMET ribbon is presented in Fig. 5 (left top). The derived distribution of hyperfine fields is centered at 20 T with a shoulder above 10 T (similar to other studies [26]) as shown in the Fig. 5 top right panel.

Both the coarse and fine fractions were collected following the exposure of the ribbons to EEW. A rather complex spectrum can be observed for the coarse fraction (Fig. 5 left, middle). At the first approach, certain crystallization can be presumed. For interpretation, the crystalline Fe-Si-B ternary phase diagram can be consulted where existence of  $\text{Fe}_3\text{B}$ ,  $\text{Fe}_2\text{Si}_{0.4}\text{B}_{0.6}$ , and bcc phases is reported at the  $x_{\text{Fe}} = 0.74$  section [27]. A close analogy can be

found with comparison to Mössbauer spectra of heat treated, partly recrystallized FINEMET ribbons with similar compositions. These spectra are interpreted with decomposition to 5–6 crystalline phases which are characterized with sharp sextets and with additional presence of certain amount of amorphous phase in the intergranular regions exhibiting distribution in the magnetic field [26, 28]. Heat treatment of the ribbon with the very same composition as used in our recent study has also been performed at 540 °C for 1 h and high-velocity-resolution room-temperature Mössbauer spectra were recorded. These spectra exhibit very similar shape as shown in Fig. 5 (left, middle). For the interpretation of spectra, six different iron sites are assumed with 4,5,6,7 and 8 nearest neighbors in different iron sites [29]. If the very same approach is used in our recent case, the decomposition results in data presented in SMbTable 3 (SI). Graphic representation of this described decomposition is presented in Fig. 5 (right bottom).

Thus, an important observation can be deduced, namely that certain part of the spectrum ( $\sim 22\%$ ) can be attributed to amorphous phase (in contrast to HITPERM, where amorphous phase was not detected).

For comparison, the Mössbauer spectrum of the fine fraction observed on the highly dispersed particles floating for several days in the aqueous suspension is also presented. Magnetic particles are present only in negligible amount, and the spectrum can be described as sum of  $\text{Fe}^{2+}$  and  $\text{Fe}^{3+}$  oxide components (Fig. 5, left, bottom).

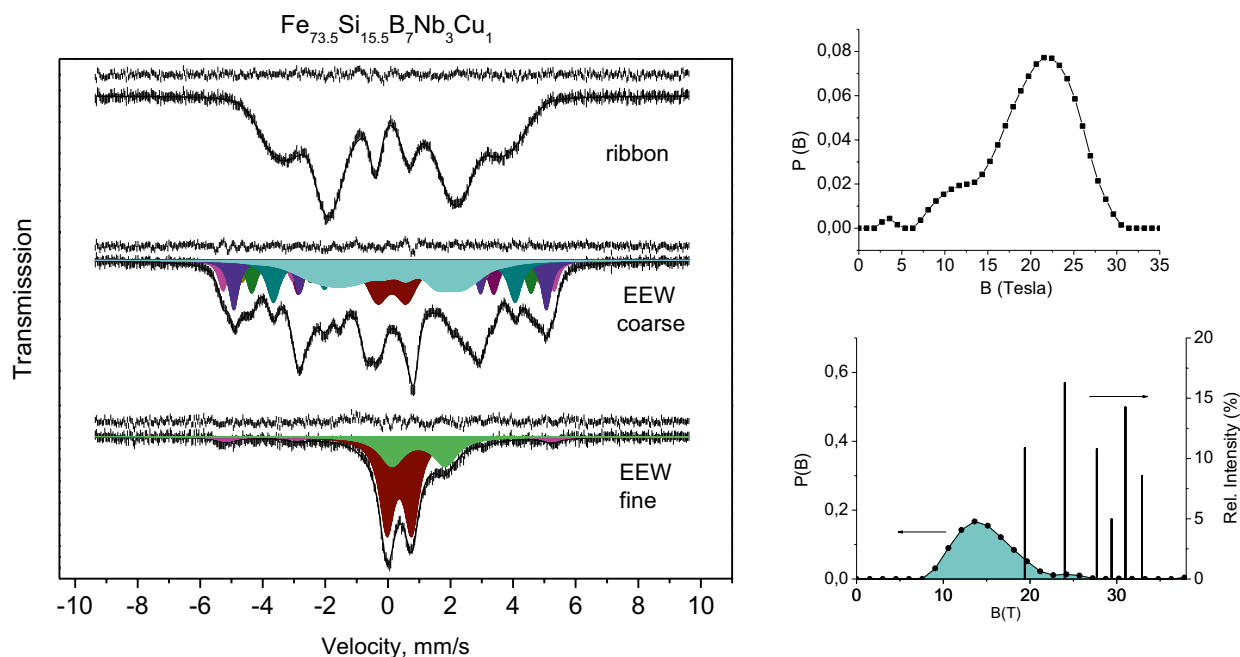


**Figure 5:** Mössbauer spectrum of FINEMET ribbon as quenched, coarse, and fine fractions after EEW (left side, top, middle, and bottom, respectively). The distribution of hyperfine fields is presented on the top right panel. The presence of crystalline phases is detected in the left middle spectrum, and the corresponding magnetic field strengths and their relative intensities are represented with vertical lines on the right bottom inset. Certain part of the spectrum can be described with a distribution of magnetic fields in connection with preservation of amorphous phase to a certain extent (marked with light green). The spectrum of fine fraction is composed from signals of oxides (left bottom).

### **Fe<sub>71.6</sub>Si<sub>3.4</sub>C<sub>12.3</sub>Mn<sub>0.6</sub>B<sub>12.2</sub>: bulk amorphous—i.e., cast iron with addition of 12% B, CiB<sub>12</sub> in short**

Characteristic feature of bulk amorphous alloys is that they solidify in amorphous state even at low cooling rate, i.e., they can be prepared with a simple casting into a mold (instead of the rapid quenching with injecting the melt to a rotating wheel.) Bulk amorphous alloys can conveniently be obtained by adding glass-forming additives (boron and silicon) to carbon-containing cast iron. Thus, CiB<sub>12</sub> notation will be used in the forthcoming part instead of the long Fe<sub>71.6</sub>Si<sub>3.4</sub>C<sub>12.3</sub>Mn<sub>0.6</sub>B<sub>12.2</sub> formula.

Water was used for cooling media in the previous instances in EEWs of ribbons, and rather vivid chemical reactions were detected during the process accompanied with expressed oxide formation as described above. To compare the influence of cooling media ethylene glycol was also used beside water with CiB<sub>12</sub> samples. In the case of ethylene glycol highly active C and O radicals may be produced in the explosion, and gaseous CO and CO<sub>2</sub> may form, decreasing the amount of O available for oxide formation.

The difference in the *morphology* of products of EEW in dependence of the cooling media is clearly manifested with the comparison of *SEM images*. In the coarse fraction collected in water, more small oxide particles are formed which are deposited on the globules, whereas the surface of the spherical

particles solidified in ethylene glycol is smooth and clean. The morphologies of fine fractions are also different and formation of carbonaceous fibers can also be observed in ethylene glycol. (See the corresponding images in the Supporting information, Fig. SSEM4).

### **XRD (recorded on coarse fractions)**

The diffractograms of the starting ribbon and the products collected after EEW in water and ethylene glycol are distinctly different. The as-cast ribbon exhibits a broad peak attesting for the amorphous state (Fig. 6 top). Having the EEW performed on the ribbons in water primarily characteristic peaks of bcc iron can be observed at  $2\Theta = 52.49, 77.41, \text{ and } 99.97$  values (Fig. 6, middle, ICDD card #87-0722). Thus, probably silicon and boron were removed via preferred oxide formation with these elements. In contrast, XRD of coarse fraction collected from ethylene glycol exhibits broad variety of peaks dominantly in the  $2\Theta$  50–55 deg region characteristic for of  $\chi$  and  $\Theta$  iron carbides (in correspondence with ICDD cards #51-0997 and #77-0255, respectively, Fig. 6 bottom).

### **HRTEM on products of EEW of CiB<sub>12</sub>: in water**

Core-shell structure is characteristic for the products with a particular feature. Namely, the outer covering layers are composed

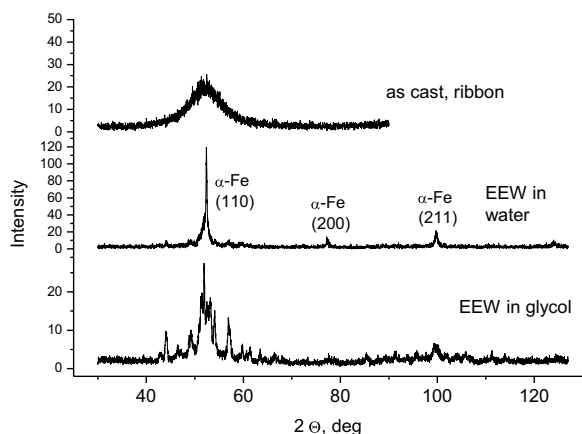


**Figure 6:** XRD diffractograms obtained on bulk amorphous  $\text{C}_i\text{B}_{12}$  ribbon (top), after EEW in water (middle) and EEW in ethylene glycol (bottom).

from two constituents—one is the iron oxide and the other is a carbonaceous outermost layer (Fig. 7). The carbonaceous outermost layer can be originated from the sample itself since carbon is present in 12 atomic percent in the starting ribbon.

The HRTEM image on the top left in Fig. 7 displays various morphologies. The top right inset in this panel is the fast Fourier transform with the spots and rings characteristic for magnetite structure. The middle and right images in the top row show the composite structure of the covering outer layers with higher magnification. The elemental distributions reflect also various

concentrations of elements in the surface regions of particles (Fig. 7 bottom row).

#### HRTEM on products of EEW of $\text{C}_i\text{B}_{12}$ in ethylene glycol

Agglomeration of covered melted and solidified globules in a wide size range can be observed in Fig. 8, left. The main iron-rich phase in the globules may contain certain amount of carbon [Fig. 8(b, c)] The elemental analysis of the outer shells of the agglomerated particles shows the presence of a double layer, the inner one is more rich in oxygen and the outer in carbon (Fig. 8 top right). Both the amorphous and ordered oxide structures can be revealed from images. The fast Fourier transform image on the central part of a spherical particle displays ring at 2.1 Å characteristic for amorphous structure [Fig. 8(e)]. In contrast, fast Fourier transformation on a thinner particle still with globular morphology is characteristic for oxide (magnetite) structure [Fig. 8(f)].

#### Mössbauer spectroscopy on products of EEW of $\text{C}_i\text{B}_{12}$ in water

For comparison, the Mössbauer spectrum of the starting  $\text{C}_i\text{B}_{12}$  ribbon is also presented, it is characteristic for a typical amorphous structure [Fig. 9(a)]. The full spectrum can be described with a distribution centered at 23.6 T, (Fig. 9 right, top), similarly to other bulk amorphous samples (e.g.,  $\text{Fe}_{61}\text{Co}_{10}\text{Y}_8\text{W}_1\text{B}_{20}$  [30] or VITROVAC [31]).

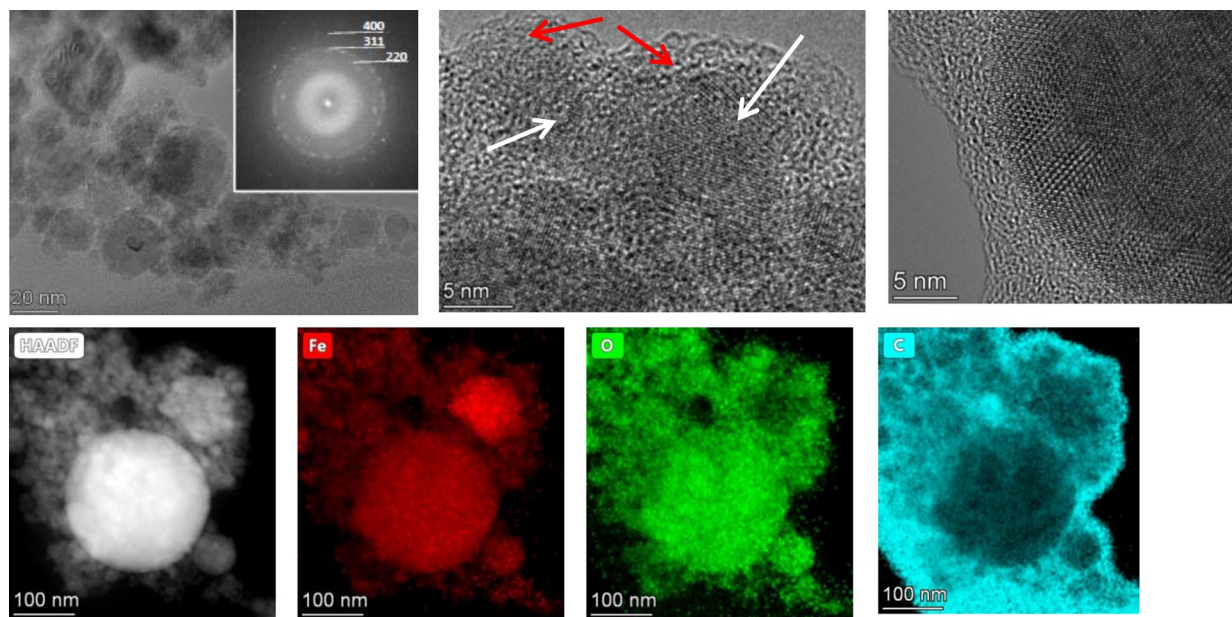


**Figure 7:** HRTEM images collected on products of  $\text{C}_i\text{B}_{12}$  exposed to EEW in water at different magnifications (top row). The inset in the left panel is the fast Fourier transform from an area of  $180 \times 180$  nm. Based on the interplanar spacings, magnetite structure is identified (Miller indices are given). The middle and right images show the ordered (oxide) and disordered (carbonaceous) components of sample. Red arrows point oxide core, white arrows point carbonaceous outer layers on particles. The bottom row displays elemental distributions.



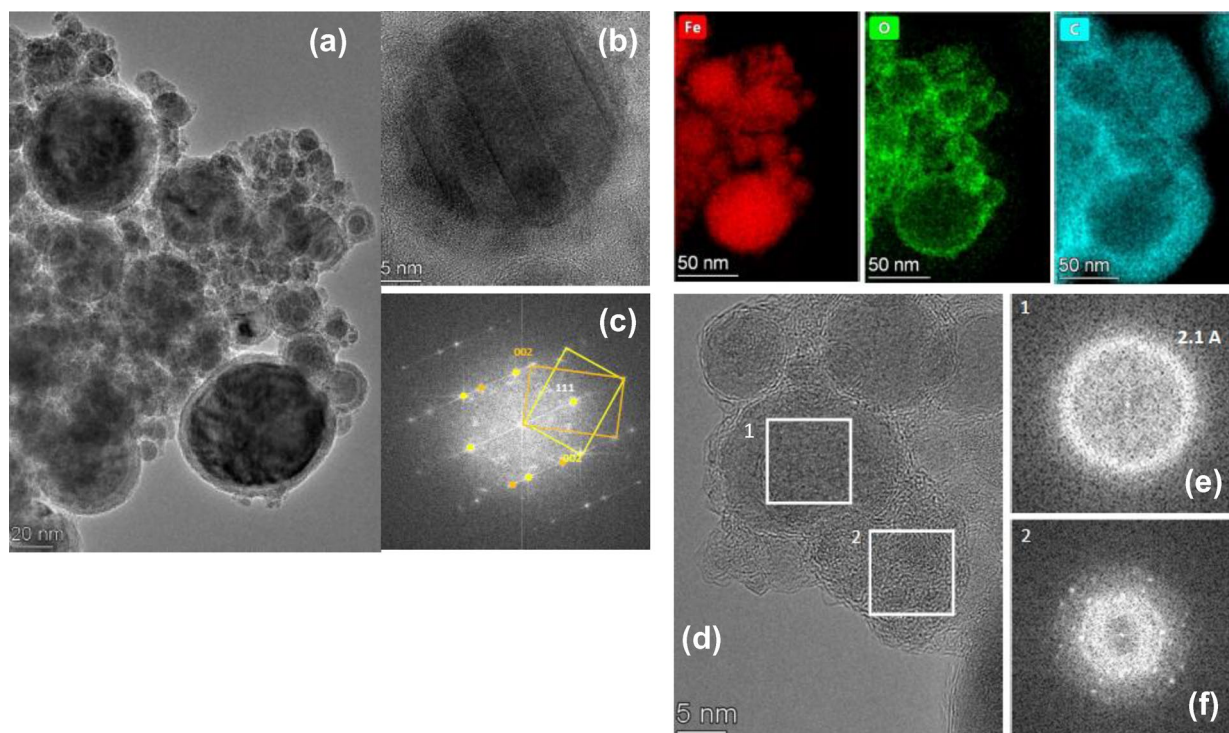


**Figure 8:** HRTEM of  $\text{CiB}_{12}$  in ethylene glycol. Left: gross image on products, (a) Twinning frequently can be observed in metal particles, (b) Fast Fourier transform of image b) attesting for the presence of twinned FCC iron or  $\text{Fe}_{15}\text{C}$ , (c) The right top part represents the elemental distributions for Fe, O, and C obtained on the region shown in (a). HRTEM image on higher magnification on spherical particles is shown in (d). FFTs obtained in selected regions #1 and #2 display a ring from amorphous structure at 2.1 Å (e), and diffraction spots from oxide, (f), respectively.

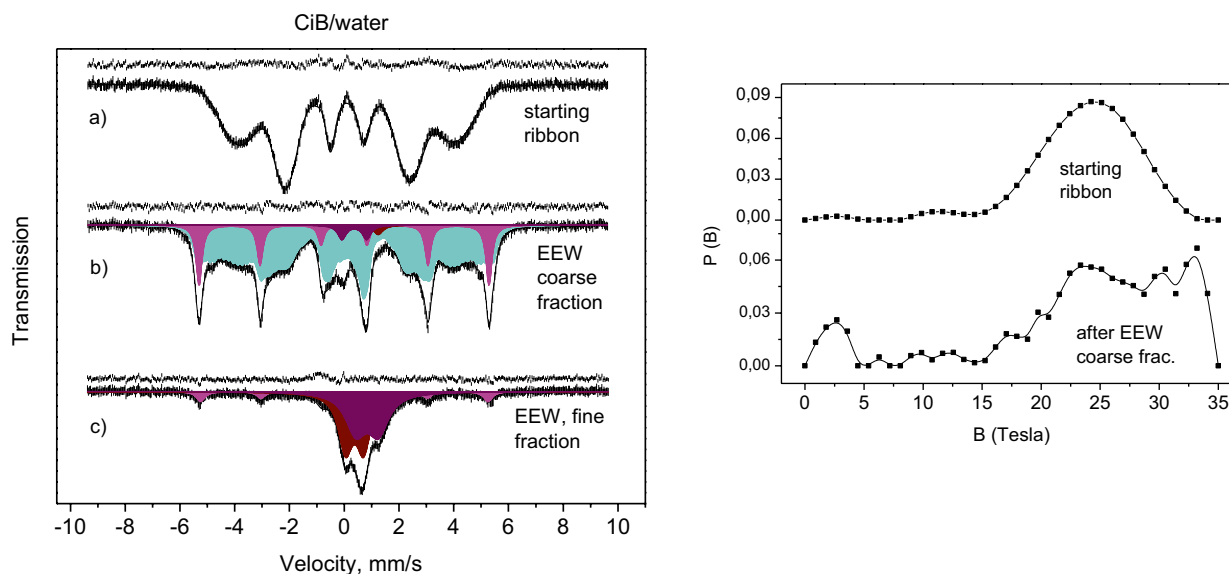


**Figure 9:** Mössbauer spectra of  $\text{CiB}_{12}$  (left side, starting ribbon (a), top), products of EEW coarse fraction (b), middle), and fine fraction (c), bottom). The right side represents the distributions of magnetic hyperfine fields (starting ribbon, top, and coarse fraction of products, bottom).

Mössbauer spectra were recorded both on the coarse and fine fractions after the EEW in water. The coarse fraction dominantly exhibits combination of a sharp sextet with a distribution. The sharp sextet has parameters close to metallic bcc iron (with

characteristic  $\delta$ , and internal magnetic hyperfine field, MHF, with 21% spectral area). Additionally 5% FeO can be identified in the spectrum [Fig. 9(b)]. The largest part of the spectrum (76% spectral area) can be described with a distribution



of magnetic fields centered at 24 Tesla. This value is the same as for the starting amorphous foil; thus, it can be attributed to preservation of amorphous state in a part inside the melted/solidified globules (Fig. 9. right, bottom).

The overwhelming part of the Mössbauer spectrum of the fine fraction can be described as oxides (42% FeO with characteristic  $\delta = 0.91$  and  $\Delta = 0.83$  mm/s, and to 44% Fe<sup>3+</sup> oxide with  $\delta = 0.35$ , and  $\Delta = 0.66$  mm/s values). Only a minor (part 14%) displays the characteristic metallic sextet of iron (Fig. 9 left, bottom). This observation is in full accordance with results of the HRTEM study in which significant presence of oxides was revealed, too.

### Mössbauer spectroscopy on products of EEW CiB<sub>12</sub> in ethylene glycol

The presence of distributions in hyperfine fields is more dominant in products of EEW in ethylene glycol. The spectrum of the coarse fraction can almost exclusively be described with a distribution (92.5% of spectral area, centered at 21.9 Tesla). The remaining part (7.5% area) can be attributed to sextet of metallic iron (see spectrum in Fig. 10, left top, and the corresponding distribution in the right top part of the figure.) The spectrum obtained on the fine fraction of products is rather complex. More than half of the spectrum can be described with distribution of hyperfine magnetic fields (53% area, centered at 19 Tesla). Quarter of this spectrum can be assigned to iron carbides (with 21.2 and 25.5 Tesla fields) together with a doublet (11% with  $\delta = 0.27$

and  $\Delta = 0.2$  mm/s values). The remaining smallest part (8%) can be assigned to metallic iron with the characteristic 33 Tesla inner magnetic field. Comparison of spectra of products collected from water and ethylene glycol clearly shows that the oxidation takes only place to a small extent in ethylene glycol, in strong contrast with water.

### Conclusions

Amorphous ribbons (HITPERM, FINEMET, and bulk amorphous cast iron, CiB<sub>12</sub>) were exposed to electric explosion process in water, and additionally in ethylene glycol for CiB<sub>12</sub>. Formation of various products in a great variety is revealed in reactions with the corresponding liquid media. In most cases, products were collected in two fractions. Morphology and surface composition of products were studied by SEM, the phases present in the coarse fractions by XRD. Mössbauer spectroscopy provided information both on the molten/solidified metallic and on the direct product (oxide) phases. Structure and composition of products in fine fractions were revealed from HRTEM analysis.

The predominant portion is the coarse fraction composed primarily from molten and solidified droplets. For this part, the interactions may take place on the surface of the small metallic droplets. The other, minor part (fine fraction,  $\approx 5\%$ ), is composed from products of reactions among vaporized metals and evaporated/decomposed cooling media. The loss of amorphous structure can be attributed in a great extent to chemical changes. In particular, preferred oxidation of glass-forming

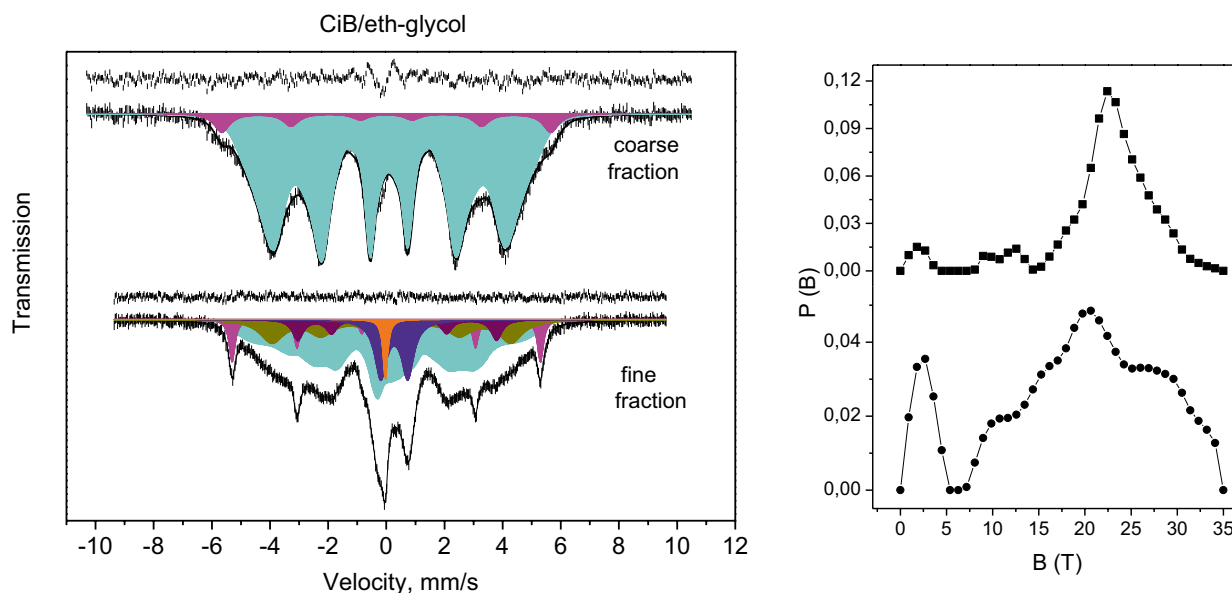


**Figure 10:** Mössbauer spectra of coarse and fine fractions collected after EEW of CiB<sub>12</sub> in ethylene glycol (left), and corresponding hyperfine field distributions (right, coarse fraction, top, fine fraction, bottom).

components (Zr, Si, B) can take place in water beside oxidation of the main components (iron and cobalt). On the other hand, certain stabilization of amorphous state can be observed in the carbon-containing media (in ethylene glycol with  $\text{CiB}_{12}$ ). The amorphous state is not sustained in HITPERM, a small part (~20%) is preserved in FINEMET whereas the highest portion is preserved in the EEW process with  $\text{CiB}_{12}$ , in accordance with the glass-forming ability of the given composition.

## Materials and methods

### Preparation of amorphous (metallic glass) ribbons

The ingots with the given compositions were prepared by induction melting in water cooled copper mould. The ribbons were prepared by rapid quenching of the re-melted ingot placed in a quartz tube. The liquid alloy obtained by inductive heating was injected to a copper disk rotating with 40 m/sec peripheral speed [32]. The widths and thicknesses of ribbons obtained from different melts varied between 2–3.5 mm and 25–35  $\mu\text{m}$ , respectively. In correspondence, their cross sections varied as well in between a factor of 2–3. Consequently, the experimental conditions were slightly different for explosion performed with the same input power.

### Electric explosion process

Melt spun ribbons, crystalline  $\text{Fe}_{50}\text{Co}_{50}$ , and amorphous  $\text{Fe}_{45}\text{Co}_{45}\text{Zr}_7\text{B}_3$  (HITPERM), and  $\text{Fe}_{73.5}\text{Si}_{15.5}\text{B}_7\text{Nb}_3\text{Cu}_1$  (FINEMET) were exposed to EEW in water. Further, to compare the influence of the cooling media on the chemical processes, EEW of bulk amorphous  $\text{Fe}_{71.6}\text{Mn}_{0.6}\text{Si}_{3.4}\text{C}_{12.3}\text{B}_{12.2}$  was carried out in two media, in water and in ethylene glycol.

Ribbons of 2 cm length were exposed to 100 J energy by discharging 200  $\mu\text{F}$  capacitors at 1 kV, resulting in a 6 kA (at maximum) current pulse within ca. 6 microsecond. The products were collected in two fractions using a strong permanent magnet, the coarse fraction was precipitated on the bottom of the discharge vessel, whereas the fine fraction was collected from the suspension of products able to float for 2–3 days. All products were completely collected in these two fractions, without any residue. Further experimental details are described in [16].

## Characterization

### HRTEM

Samples for the TEM analysis were prepared by suspending the products in ethanol. A drop of suspension was deposited onto lacey carbon coated copper TEM grid (Ted Pella). TEM analysis was performed at 200 keV accelerating voltage using an FEI Themis 200 TEM with a Cs corrected objective lens (Schottky FEG electron source, point resolution is 0.8 nm in

HRTEM (High-Resolution Transmission Electron Microscopy) mode and 0.16 nm in STEM (Scanning Transmission Electron Microscopy) mode equipped with FEI Super-X EDS detection system. Areas for EDS mapping were selected using HAADF (High-Angle Annular Dark Field) images in STEM mode. HRTEM image, as well as EDS spectrum images, were recorded by a 4kx4k Ceta camera using Velox software (Thermo Fischer).

For identification of the crystalline phase of the nanoparticles, zone axis orientation and characteristic interplanar spacings ( $d$  values) were determined based on the fast Fourier transforms (FFT) of the atomic resolution images. Offline Fourier transformation and pixel-by-pixel post processing of the spectrum images was done using the Velox software (Thermo Fischer).

### X-ray diffraction measurements

A theta–theta type Bruker D8 Advance diffractometer was used where the  $\text{Co-K}_\alpha$  radiation (wavelength  $\lambda = 0.17890$  nm) is reflected from the free surface of the specimen and reaches the detector through a graphite monochromator in the diffraction beam. The scanning voltage of the X-ray tube was 40 kV, the current was 40 mA, and a  $0.25^\circ/\text{min}$  scanning rate was applied in the  $2\Theta$  angle region of  $35^\circ$ – $103^\circ$ .

### Scanning electron microscopy (SEM)

This method was used to study the morphologies and compositions of the samples. Samples were investigated using a JEOL JSM-5600LV scanning electron microscope. The chemical compositions of the particles were determined by energy dispersive X-ray analysis (EDS2000, IXRF Systems), with 15 kV acceleration voltage (for the bulk amorphous alloy with 25 kV) and  $\times 35$  to  $\times 500$  magnifications were used in image recording and elemental analysis modes. Due to the low accelerating voltage of electrons, the elemental analysis provides information on the composition of top layer of particles in 3–4 micron depth.

### Mössbauer spectroscopy

Spectra were collected in constant acceleration mode on a KFKI spectrometer at room temperature equipped with a 1 GBq activity  $^{57}\text{Co}/\text{Rh}$  source. Spectra were recorded in 1000 channels and were folded afterwards. Isomer shift values are given relative to the center of the sextet spectrum of metallic  $\alpha$ -iron at room temperature with typical line widths of 0.24 mm/s. The accuracy of the positional parameters (isomer shift,  $\delta$ , and quadrupole splitting,  $\Delta$ ) is ca.  $\pm 0.03$  mm/s. Spectra were evaluated using MossWinn code by using Lorentzian line shape [33]. Quality of fits were judged based on the corresponding relative  $\chi^2$  values,

and reasonable fits with the lowest relative  $\chi^2$  were selected. The highest value of  $\chi^2$  in the presented spectra is below 1.7.

## Acknowledgments

The authors are thankful to T. Fekete for performing the SEM measurements and evaluation of the related data on products of EEW on Fe<sub>50</sub>Co<sub>50</sub> and HITPERM and FINEMET ribbons.

## Funding

Open access funding provided by Centre for Energy Research.

## Data availability

Data and images collected in measurements are available upon reasonable requests.

## Declarations

**Conflict of interest** The authors declare no conflicts of interests related to the present communication.

## Supplementary Information

The online version contains supplementary material available at <https://doi.org/10.1557/s43578-022-00771-3>.

## Open Access

This article is licensed under a Creative Commons Attribution 4.0 International License, which permits use, sharing, adaptation, distribution and reproduction in any medium or format, as long as you give appropriate credit to the original author(s) and the source, provide a link to the Creative Commons licence, and indicate if changes were made. The images or other third party material in this article are included in the article's Creative Commons licence, unless indicated otherwise in a credit line to the material. If material is not included in the article's Creative Commons licence and your intended use is not permitted by statutory regulation or exceeds the permitted use, you will need to obtain permission directly from the copyright holder. To view a copy of this licence, visit <http://creativecommons.org/licenses/by/4.0/>.

## References

1. W.G. Chace, H.K. Moore (eds.), *Exploding Wires* (Plenum Press, New York, 1968)
2. A.V. Pervikov, Metal, metal composite and composited nanoparticles obtained by electrical explosion of wires. *Nanobiotechnol. Rep.* **16**, 401–420 (2021). <https://doi.org/10.1134/S2635167621040091>
3. V.I. Oreshkin, R.B. Bakhst, Wire explosion in vacuum. *IEEE Trans. Plasma Sci.* **48**, 1214–1248 (2020). <https://doi.org/10.1109/TPS.2020.2985100>
4. M. Bigelmayr, P. Pieterse, D. Uhrlandt, Energy dissipation and efficiency of exploding stainless steel wires of various lengths and diameters. *J. Phys. D: Appl. Phys.* **54**, 045202 (2021). <https://doi.org/10.1088/1361-6463/abbe4c>
5. D. Qian, Z. Liu, L. Li, X. Zou, X. Wang, Observation of early stage of underwater electrical wire explosion by shadowgraph. *IEEE Access* **8**, 85968–85972 (2020). <https://doi.org/10.1109/ACCESS.2020.2992284>
6. V.M. Romanova, G.V. Ivanenkov, A.R. Mingaleev, A.E. Ter-Oganesyan, T.A. Shelkovenko, S.A. Pikuz, Electric explosion of fine wires: Three groups of materials. *Plasma Phys. Rep.* **41**, 617–636 (2015). <https://doi.org/10.1134/S1063780X15080085>
7. R. Han, J. Ju, W. Ding, H. Zhou, A. Qiu, Y. Wang, A comparison study of exploding a Cu wire in air, water, and solid powders. *Phys. Plasmas* **24**, 113515 (2017). <https://doi.org/10.1063/1.5003769>
8. S. Ghosh, P. Ranjan, A. Kumaar, R. Sarathi, S. Ramaprabhu, Synthesis of titanium carbide nanoparticles by wire explosion process and its application to carbon dioxide adsorption. *J. Alloys Compd.* **794**, 645–653 (2019). <https://doi.org/10.1016/j.jallcom.2019.04.299>
9. P. Ranjan, T. Kurosaki, H. Suematsu, R. Jayaganthan, R. Sarathi, Formation of tungsten carbide nanoparticles by wire explosion process. *Appl. Ceram. Technol.* **17**, 304–310 (2020). <https://doi.org/10.1111/ijac.13350>
10. M.I. Lerner, A.S. Lozhkomoev, A.V. Pervikov, O.V. Bakina, Synthesis of Al-Al<sub>2</sub>O<sub>3</sub> and Al-AlN nanoparticle composites via electric explosion of wires. *Russ. Phys. J.* **59**, 422–429 (2016). <https://doi.org/10.1007/s11182-016-0789-5>
11. Q. Wang, M. Guo, C. Li, Rapid fabrication and characterization of spherical Mumetal nanoparticles by an electrical explosion process. *Integr. Ferroelectr.* **172**, 49–58 (2016). <https://doi.org/10.1080/10584587.2016.1175878>
12. O. Bakina, E. Glazkova, A. Pervikov, A. Lozhkomoev, N. Rodkevich, N. Svarovskaya, M. Lerner, L. Naumova, E. Varnakova, V. Chjou, Design and preparation of silver-copper nanoalloys for antibacterial applications. *J. Clust. Sci.* **32**, 779–786 (2020). <https://doi.org/10.1007/s10876-020-01844-1>
13. A.D. Rud, N.I. Kuskova, L.I. Ivaschuk, G.M. Zelinskaya, N.M. Biliy, Structure state of carbon nanomaterials produced by high-energy electric discharge techniques. *Fuller. Nanotubes Carbon Nanostruct.* **19**, 120–126 (2011). <https://doi.org/10.1080/1536383X.2010.490129>
14. L. Zuo, X. Li, T. Zhang, General route to fabricate ultrafine metallic glass powders directly from their own crystalline states by localized pulsed electrical discharge atomization. *Intermetallics* **136**, 107267 (2021). <https://doi.org/10.1016/j.intermet.2021.107267>



15. D. Zhang, W. Choi, Y. Oshima, U. Wiedwald, S.-H. Cho, H.-P. Lin, Y.K. Li, Y. Ito, K. Sugioka, Magnetic Fe@FeO<sub>x</sub>, Fe@C, and α-Fe<sub>2</sub>O<sub>3</sub> single-crystal nanoblends synthesized by femtosecond laser ablation of Fe in acetone. *Nanomaterials* **8**, 631 (2018). <https://doi.org/10.3390/nano8080631>
16. K. Lázár, L.K. Varga, V. Kovács Kis, T. Fekete, Z. Klencsár, S. Stichleitner, L. Szabó, I. Harsányi, Electric explosion of steel wires for production of nanoparticles: Reactions with the liquid media. *J. Alloys Compd.* **763**, 759–770 (2018). <https://doi.org/10.1016/j.jallcom.2018.05.326>
17. M. Ghafari, W.D. Hutchison, S.J. Campbell, H. Gleiter, H. Hahn, T. Feng, Electrical resistivity and wave character of free electrons in amorphous and nanoglass Sc<sub>75</sub>Fe<sub>25</sub>. *J. Phys. Condens. Matter* **30**, 025702 (2018). <https://doi.org/10.1088/1361-648X/aa9adf>
18. I. Ogasawara, S. Ueno, Preparation and properties of amorphous wires. *IEEE Trans. Magn.* **31**, 1219–1223 (1995)
19. I.V. Beketov, R. Pérez, A.V. Bagazeev, M. Vazquez, A.I. Medvedev, A. Safronov, G.V. Kurlandskaya, Magnetic nanoparticles of (Co<sub>0.94</sub>Fe<sub>0.06</sub>)<sub>72.5</sub>Si<sub>12.5</sub>B<sub>15</sub> and Fe<sub>78</sub>Si<sub>9</sub>B<sub>13</sub> obtained by electric explosion of amorphous wires. *Key Eng. Mater.* **644**, 203–206 (2015). <https://doi.org/10.4028/www.scientific.net/KEM.644.203>
20. S.-X. Liang, S. Salamon, S. Zerebecki, L.-C. Zhang, Z. Jia, H. Wende, S. Reichenberger, S. Barcikowski, A laser-based synthesis route for magnetic metallic glass nanoparticles. *Scr. Mater.* **203**, 114094 (2021). <https://doi.org/10.1016/j.scriptamat.2021.114094>
21. S.-X. Liang, L.-C. Zhang, S. Reichenberger, S. Barcikowski, Design and perspective of amorphous metal nanoparticles from laser synthesis and processing. *Phys. Chem. Chem. Phys.* **23**, 11121–11154 (2021). <https://doi.org/10.1039/D1CP00701G>
22. J.E. Frackowiak, Determination of the long-range order parameter in the transition metal alloys using Mössbauer spectroscopy. *phys. Stat. Sol. (a)* **87**, 109 (1985)
23. B. deMayo, D.W. Forester, S. Spooner, Effects of atomic configurational changes on hyperfine interactions in concentrated iron-cobalt alloys. *J. Appl. Phys.* **41**, 1319–1320 (1970). <https://doi.org/10.1063/1.1658920>
24. <https://webbook.nist.gov/chemistry>. Accessed May 2022.
25. M. Migliorini, Hyperfine interactions and crystallization kinetics of co-substituted NANOPERM-type alloys. *J. Phys.: Conf. Ser.* **217**, 012092 (2010). <https://doi.org/10.1088/1742-6596/217/1/012092>
26. J.M. Borrego, A. Conde, V.A. Pena-Rodriguez, J.M. Greneche, A fitting procedure to describe Mössbauer spectra of FINEMET-type nanocrystalline alloys. *Hyperfine Interact.* **131**, 67–82 (2000)
27. M.G. Poletti, L. Battezzati, Assessment of the ternary Fe-Si-B phase diagram. *CALPHAD: Comput. Coupling Phase Diagr. Thermochem.* **43**, 40–47 (2013). <https://doi.org/10.1016/j.calphad.2013.08.001>
28. J.-M. Greneche, M. Migliorini, A. Slawska-Waniewska, Iron-based nanocrystalline alloys investigated by <sup>57</sup>Fe Mössbauer spectrometry. *Hyperfine Interact.* **126**, 27–34 (2000)
29. M.I. Oshtrakh, Z. Klencsár, V.A. Semionkin, E. Kuzmann, Z. Homonnay, L.K. Varga, Annealed FINEMET ribbons: Structure and magnetic anisotropy as revealed by the high velocity resolution Mössbauer spectroscopy. *Mater. Chem. Phys.* **180**, 66–74 (2016). <https://doi.org/10.1016/j.matchemphys.2016.05.032>
30. M. Nabialek, Influence of the quenching rate on the structure and magnetic properties of the Fe-based amorphous alloy. *Arch. Metall. Mater.* **61**, 439–444 (2016). <https://doi.org/10.1515/amm-2016-0079>
31. S.N. Kane, A. Gupta, L.K. Varga, Mössbauer study of plastic deformation in amorphous Fe<sub>40</sub>Ni<sub>40</sub>B<sub>20</sub> and Fe<sub>78</sub>Si<sub>9</sub>B<sub>11</sub>C<sub>2</sub> alloys. *J. Magn. Magn. Mater.* **254–255**, 501–503 (2003)
32. Á. Révész, A. Concustell, L.K. Varga, S. Surinach, M.D. Baró, Influence of the wheel speed on the thermal behaviour of Cu<sub>60</sub>Zr<sub>20</sub>Ti<sub>20</sub> alloys. *Mater. Sci. Eng. A* **375–377**, 776–780 (2004)
33. Z. Klencsár, MossWinn Manual. <http://www.mosswinn.hu/downloads/mosswinn.pdf>. Accessed Feb 2019